NIH Public Access
Author Manuscript
Biochemistry. Author manuscript; available in PMC 2014 November 12.

Published in final edited form as:
Biochemistry. 2013 November 12; 52(45): 7943–7950. doi:10.1021/bi401118q.

Functional Consequences of the Open Distal Pocket of Dehaloperoxidase-Hemoglobin Observed by Time-Resolved X-ray Crystallography

Junjie Zhao[1], **Vukica Srajer**[2,†], and **Stefan Franzen**[1,*,†]

[1]Department of Chemistry, North Carolina State University, Raleigh, NC 27695, USA

[2]Center for Advanced Radiation Sources, The University of Chicago, Chicago, IL 60637, USA

Abstract

Using time-resolved X-ray crystallography, we contrast a bifunctional dehaloperoxidase-hemoglobin (DHP) with previously studied examples of myoglobin and hemoglobin in order to understand the functional role of the distal pocket of globins. One key functional difference between the DHP and other globins is the requirement that H_2O_2 enter the distal pocket of oxyferrous DHP in order to displace O_2 from the heme Fe atom and thereby activate the heme for the peroxidase function. The open architecture of DHP permits more than one molecule to simultaneously enter the distal pocket of the protein above the heme in order to facilitate the unique peroxidase cycle starting from the oxyferrous state. The time-resolved X-ray data show that the distal pocket of DHP lacks a protein valve found in the two other globins that have been studied previously. The photolyzed CO ligand trajectory in DHP does not have a docking site. Rather the CO moves immediately to the Xe-binding site. From there CO can escape, but also recombine an order of magnitude more rapidly than in other globins. The contrast with DHP dynamics and function more precisely defines the functional role of the multiple conformational states of myoglobin. Taken together with the high reduction potential of DHP, the open distal site helps to explain how a globin can also function as a peroxidase.

Keywords

Molecular Dynamics; Peroxidase; Hemoglobin; Xe binding site; Carbon monoxide

Trajectories of diatomic ligands in heme proteins have provided a wealth of information on how such molecules can enter and exit the protein, which must fluctuate in order to permit their passage. The time-resolved X-ray crystallography technique has provided the most detailed images of the transport of the carbon monoxide ligand (CO) to various cavities within proteins (1–5). However, the function of protein cavities is still an open question. Indeed, it is difficult to assign a general function based on the analysis of a single protein, since the functional role of cavities may vary from one protein to another. Thus far, two heme proteins, Sperm Whale

*To whom correspondence should be addressed: Stefan Franzen, Department of Chemistry, North Carolina State University, Raleigh, NC 27695, Stefan_Franzen@ncsu.edu, Phone: 919-515-8915.

†**Funding.** The authors thank the Army Research Office for support through grant LS-57681. Use of the Advanced Photon Source was supported by the U.S. Department of Energy, Basic Energy Sciences, Office of Science, under Contract No. DE-AC02-06CH11357. Use of the BioCARS Sector 14 was supported by the National Institutes of Health, National Institute of General Medical Sciences grant P41GM103543 (formerly National Center for Research Resources P41RR007707).

ACCESSION NUMBERS: Coordinates and structure factors have been deposited in the Protein Data Bank with accession number 4JYQ.

Supporting Information: Time-resolved X-ray Crystallographic Data Reduction Statistics, Refinement statistics for the dark DHP-CO crystal structure and an alternative view of Figure 1 with a white background are presented. These materials are available free of charge at http://pubs.acs.org.

NIH-PA Author Manuscript
NIH-PA Author Manuscript
NIH-PA Author Manuscript

NIH-PA Author Manuscript

NIH-PA Author Manuscript

NIH-PA Author Manuscript

myoglobin (SWMb) (2–3) and *Scapharca inaequivalvis* dimeric hemoglobin (HbI) (4–5), have been the most extensively studied by time-resolved crystallography. Although one is a myoglobin and the other a hemoglobin they both have the reversible binding of O_2 as their primary function. Despite the rich set of conformational changes associated with the allosteric cooperative transition in photolyzed HbI*CO, the nature of the CO trajectory in that globin has certain similarities with SWMb*CO (The asterisk indicates a photolyzed carbon monoxide molecule, following photon absorption by the heme that leads to rupture of the Fe-CO bond). Both have a distal docking site B, where the initially photolyzed CO molecule resides. The B-site in both proteins is a distinct ligand docking site in the distal pocket, not observed as the Xe binding site in either proteins. (2, 4) Based on experiments designed to block the Xe-binding cavities in SWMb*CO and HbI*CO, and on time-resolved crystallographic studies, it has been deduced that the cavities in these proteins do not constitute an exit route for diatomic ligands (6–7). Instead, exit occurs near the distal histidine in both SWMb*CO and HbI*CO. Moreover, previous temperature derivative spectroscopy (TDS) studies show the presence of a nearby docking site and one or more further secondary sites in SWMb (8–10) and HbI (11) where photolyzed CO molecules can reside. Why then does CO migrate to a number of Xe-binding cavities in these proteins after it leaves the B-site? This fundamental question has been studied extensively in SWMb using many spectroscopic techniques including TDS and methods such as kinetic hole burning (12), which makes the connection between the conformation-dependent energy of recombination and the spectroscopic energy of a heme charge transfer band. In this study we propose that in order to understand the possible function of the cavities in various heme proteins, it is necessary to compare a protein with a significant difference in function. We conclude that ligand dynamics studied by time-resolved X-ray and the protein cavity in DHP identified by a Xe binding site (13) are consistent with an open architecture in the distal pocket of the bifunctional hemoglobin, DHP, which explains how it can carry out multiple functions. These features distinguish DHP from the more specialized oxygen transport proteins SWMb and HbI.

Dehaloperoxidase-hemoglobin (DHP), first isolated from the terebellid polychaete *Amphitrite ornata*, is a bifunctional protein, which displays significant peroxidase activity under physiological conditions, while also having a globin fold and an associated oxygen transport function (14). As a hemoglobin, DHP can reversibly bind with O_2 and as a peroxidase, DHP can oxidize 2,4,6-trihalophenol into the corresponding 2,6-dihaloquinone in the presence of H_2O_2. However, normal peroxidase function inactivates the ability of DHP to bind oxygen leading to a paradox because of the failure of the DHP hemoglobin function. (15) Recently, this functional paradox of DHP has been resolved by establishing that oxyferrous DHP can serve as the resting state of the peroxidase reaction cycle. (16–17) For a typical peroxidase, e.g. Horseradish Peroxidase and Cytochrome c Peroxidase, the ferric state of the heme Fe is the resting state. Thus, DHP appears to have a new type of peroxidase cycle, a ferrous peroxidase cycle. (15) Although it has high peroxidase activity, the oxyferrous peroxidase cycle and unique internal binding sites possessed by DHP distinguish it from other heme peroxidases. (18–19) The replacement of O_2 bound to the heme Fe by H_2O_2 required by the ferrous peroxidase mechanism suggests DHP must simultaneously accommodate both O_2 and H_2O_2 in the distal pocket in order to function. This requirement is quite different from other well-studied hemoglobins and myoglobins. For example, SWMb, which is by far the best studied protein, cannot simultaneously accommodate both CO and H_2O in the distal pocket (20–22). The reasons for this may become clearer in comparison with the bifunctional protein, DHP, which has a different requirement for the function of the distal pocket, namely entry of multiple molecules both for activation and for inhibition of enzymatic function. In order to address the dynamics of diatomic ligands in DHP, we have conducted a time-resolved X-ray crystallography study of the trajectory of photolyzed carbon monoxide in DHP*CO. The time-dependent structures reveal a qualitatively different CO trajectory than those observed previously in SWMb*CO and HbI*CO.

NIH-PA Author Manuscript

NIH-PA Author Manuscript

NIH-PA Author Manuscript

Materials and Methods

Sample preparation

Ferric DHP A solution was reduced by 20-fold excess sodium dithionite first and DHP-CO complex crystals (space group $P2_12_12_1$ with unit cell size a=58.90, b=68.59, c=69.35 Å) were grown by hanging-drop vapor-diffusion method from 0.2 M ammonium sulfate and 29% polyethylene glycol 8000 at 277 K in 1 atm CO atmosphere. The starting protein concentration was 8 mg ml^{-1} in 20 mM Na cacodylate pH 6.5 buffer. The crystals were transferred and mounted in 1.0 mm quartz capillaries quickly. A drop of stabilizing solution with saturated sodium dithionate was added into capillaries to remove excess O_2 before capillaries were sealed.

Time-resolved Data Collection

Time-resolved Laue X-ray diffraction experiments were conducted at BioCARS beamline 14ID at the Advanced Photon Source (23) at room temperature by using the pump-probe technique (3). For reaction initiation, we used 480 nm laser pulses from a Spectra-Physics Spitfire Pro picosecond laser coupled to a TOPAS optical parametric amplifier. The laser pulse duration was 35 ps (full width at half maximum). The laser beam size at the sample was 110 × 550 μm^2 and laser pulse energy density was 2.7 mJ/mm^2. The reaction was probed by a single, polychromatic and delayed X-ray pulse of 100 ps duration. The X-ray beam size was 90 μm (horizontal) × 70 μm (vertical) (full width half maximum). Laser and X-ray beams were perpendicular to each other as described in Figure 1 of Graber et al., 2011(23). Given the limited laser penetration depth due to the high optical density of the crystal, for each crystal orientation X-ray pulses probed only a 70 μm-deep layer of the crystal on the laser-illuminated side of the crystal. For such positioning of the crystal in the X-ray beam, for each crystal orientation a crystal edge was scanned through the X-ray beam and resulting X-ray diffraction used to guide the crystal positioning. At a fixed angular setting of the crystal, a time series of X-ray diffraction images was recorded using the same crystal volume. The time series consisted of a dark image (laser off) and images at laser-X-ray time delays of 100 ps, 1 ns, 10 ns, 1 μs, 10 μs and 1 ms. The zero time delay refers to the overlap of the leading edges of the pump, laser pulse and the probe, X-ray pulse. Pump-probe exposure (or just probe in laser off case) was repeated 5 times prior to the detector readout, in order to improve the signal-to-noise ratio of recorded diffraction patterns. Wait time between consecutive laser pulses was 0.3 s to permit the complete dark state recovery between the laser pulses and to facilitate heat dissipation. Before collecting a time series for the next angular setting of the crystal, crystal was translated slightly to expose partially fresh crystal volume to the X-ray beam, thus minimizing radiation damage. This was repeated for 42 crystal orientations, with 3° increment between angular settings of the crystal. The entire time series was collected on one crystal in order to obtain best difference maps between light and dark states. See Graber et al., 2011 (23) for more detailed description of the experiment set up and data collection geometry. The visible absorption spectrum of the crystal was taken after the X-ray data collection using the off-line BioCARS micro-spectrophotometer. The spectrum confirmed that the crystal consisted of a DHP-CO complex, with no ferric DHP present.

Time-resolved Data Processing

Laue data were processed by using the programs PRECOGNITION/EPINORM ((24) www.renzresearch.com) for scaling. All data sets were integrated to 1.8 Å and data reduction statistics are summarized in Table S1 (see SI Appendix). The reference, dark-state DHP-CO structure (PDB 4JYQ) was refined against the room temperature dark Laue data set, using the metaquo DHP structure (PDB 2QFK) as the starting model for the refinement in Refmac, CCP4 (25–26). The final model of DHP-CO structure contained two identical protein molecules

NIH-PA Author Manuscript

NIH-PA Author Manuscript

NIH-PA Author Manuscript

(chain A and chain B) in the asymmetric unit, which is the same dimeric form observed in the metaquo DHP structure. The final values of R_{cryst} and R_{free} were 15.9% and 21.2%, respectively. Refinement statistics are summarized in Table S2 (see SI Appendix). Weighted time-dependent difference maps were calculated from weighted difference structure factor (SF) amplitudes $\Delta F_w = w(|F_{DHP*}(t)| - |F_{DHP-CO}|)$ and phases derived from the reference DHP-CO structure. $|F_{DHP-CO}|$) are the dark-state SF amplitudes and $|F_{DHP*}(t)|$ are the corresponding time-dependent SF amplitudes of the photoproduct at time t (27). The weight w was calculated as (27)

$$w=1/(1+\Delta F^2/\langle|\Delta F|\rangle^2+{\sigma_{\Delta F}}^2/\langle\sigma_{\Delta F}\rangle^2)$$

where $\Delta F = |F_{DHP*}(t)| - |F_{DHP-CO}|$ is the difference of the structure factor amplitudes between time t and the dark state. $\sigma_{\Delta F}^2 = \sigma^2(F_{DHP-CO}) + \sigma^2(F_{DHP*}(t))$ is the variance of ΔF, sum of the variances of F_{DHP-CO} and $\langle x\rangle$. The symbol denotes the mean value of all values of x in a data set. Difference electron density maps for the heme region (subunit A) for different time delays, as displayed in XtalView(28), are shown in Figure 1. Maps are contoured at ±3σ and ±5σ, where σ is the root-mean-square value of the difference electron density across the asymmetric unit. Selected regions of the difference electron density maps were integrated by the program PROMSK (3) by summing up the density at grid points within a certain radius around a specific set of coordinates (5). A radius of 1.2 Å around C and O coordinates was used to determine the time dependence of the negative density at the CO binding site. In case of the positive density at the CO primary docking site (Xe1), a single sphere was used, centered at the density observed at 100 ps and with a larger radius of 1.4 Å. Integrated difference electron densities at the CO binding site and at the CO Xe1 site are shown in Figure 2.

Molecular Dynamics simulation of photolysis DHP-CO

The NAMD code (29) was used to study trajectories of photolyzed CO in DHP. The simulation parameters consisted of a time step of 2 fs consistent with application of the RATTLE algorithm (30), a cutoff of 12 Å, and a switching distance of 1.5 Å. The DHP protein was surrounded by 9254 H_2O molecules in a box with dimensions 60 × 58 × 62 Å. The particle mesh Ewald approach was used to calculate electrostatic contributions to the potential. (31) The force field used was the CHARMM27 force field. A monomer DHP protein taken originally from the 2QFK crystal structure (32) was minimized and equilibrated for 1 ns. Subsequently production dynamics were run for 20 ns. Both of the distal histidine (H55) tautomers (ε- and δ-) were studied in parallel simulations in otherwise identical systems.

Results and Discussion

Observation of Photolyzed Ligand Trajectory and Rapid Recombination in DHP*CO

Short laser pulses (~35 ps) at 480 nm were used to photodissociate CO molecule and the resulting DHP*CO photoproducts were probed by 100 ps X-ray pulses at various time delays following the laser pulses (for experimental details see Materials and Methods). Difference Fourier maps corresponding to six time delays (100 ps, 1 ns, 10 ns, 1 μs, 10 μs, 1 ms) (Figure 1A to F) reveal the differences between the average structure at a time delay t, DHP*CO (t), and the structure of the dark-state, DHP-CO (PDB 4JYQ). An alternative view of Figure 1 with a white background is provided in the Supporting Information (Figure S1). Integration of the negative difference electron density at 100 ps at the CO bound location (labeled P in Fig 1) indicates that ~11.3% of the CO is photodissociated (average value of subunits A and B, shown in Figure 2). The magnitude of feature P decreases with time as photodissociated CO (CO) rebinds with a time constant of the order of magnitude τ ~ 1 μs (Figure 2). The positive features

NIH-PA Author Manuscript

NIH-PA Author Manuscript

NIH-PA Author Manuscript

circled and labeled G in difference maps with time delays 100 ps (Figure 1A), 1 ns (Figure 1B) and 10 ns (Figure 1C) correspond to the CO located in the Xe1 docking site (a trace of this feature is also present at 1μs, Figure 1D). The coordinates for the photolyzed CO molecule are given in pdb format in the Supporting Information. Unlike SWMb, which has 4 Xe binding sites, there is only one identifiable Xe binding site inside DHP (Xe1). (13) Although the result in Figure 1 may appear similar to the trajectories in SWMb*CO (2–3, 34), there are major differences, which are related to the difference in function of DHP. The open distal pocket of DHP, which permits the binding of molecules as large as 2,4,6-tribromophenol (2,4,6-TBP) inside the globin (35) means that there is less hindrance to ligand escape, but also less hindrance for ligand entry and binding to the heme Fe. One piece of evidence for this difference is the lag in the decrease of integrated negative density P relative to the decrease in positive density G at the Xe1 docking site (Figure 2), which suggests that CO has at least partially escaped from the protein on the time scale from 10 ns and 10 μs. The observation of CO escape in the crystal is consistent with the fact that the geminate yield in DHP A is essentially zero in solution. At ambient temperature in aqueous solution the yield for CO escape in DHP-CO is ~1 compared to 0.96 in SWMbCO (33).

Comparison of the CO trajectory in DHP*CO and SWMb*CO

Figure 3A shows that the docking site of the CO coincides with the Xe binding site Xe1 in DHP. Integration of difference electron density at docking site (Xe1) in the ρ(DHP*CO) − ρ (DHP-CO) difference map (average of subunit A and B) at 100 ps indicates that about 70% of CO is located in Xe1 (Figure 2). The remaining ~30% of CO at 100 ps could not be located above 3σ, thus further migration of CO beyond the Xe1 docking site could not be detected. These results indicate that DHP possesses a significantly different CO migration pathway than that observed in photolyzed SWMb*CO. In the first place, CO recombination with the heme Fe is completed ~10 times faster in DHP (~10 μs) than in wt Mb (~100 μs). (1, 34) The difference in the CO migration pathway in DHP*CO relative to SWMb*CO results from structural differences evident in the Xe crystal structures of the respective proteins. To understand the differences we can compare the Xe occupancies in the various sites of SWMb and DHP X-ray crystal structures in the presence of high pressure Xe. There are four Xe binding sites observed in SWMb, with Xe1 site close to fully occupied in the X-ray structure, and sites Xe2-Xe4 occupied by Xe at 40–50% (36). In DHP only one internal Xe binding site is present, occupied at ~40%, with a second site that has only ~10% occupation located on the surface of the protein (13). The DHP Xe1 binding site is above the heme and coincides with the CO density at 100 ps (Figure 3A). In contrast to DHP, the largest Xe binding site in SWMb, Xe1, is on the proximal side of the heme (36). While in DHP photodissociated CO remains at the Xe1 binding site of DHP (Figure 3A), in SWMb CO migrates from the primary distal docking site B to more remote cavities Xe4 to Xe1 in a temperature-dependent manner (2–3, 34). In order to relate the migration of CO in the photolyzed X-ray crystal structures to the different functions of DHP and SWMb, we need to differentiate between the initially occupied docking site of SWMb and the protein cavities that are identified by Xe binding crystal structures.

We can distinguish between a cavity, which is identified by occupancy of a Xe atom in an X-ray crystal structure and a docking site, which is a transiently formed volume that can accommodate a photolyzed CO ligand. In DHP*CO the photolyzed CO ligand migrates directly to the Xe1 binding site, which is a permanent cavity in the protein. There appears to be no hindrance to ligand migration in the distal pocket of DHP. On the other hand, the primary CO docking site B in SWMb*CO is close to the location where a water molecule resides in the deoxy Mb distal pocket (34) and not coincident with any of the SWMb Xe binding sites. From the primary site, the CO molecule proceeds to the proximal Xe1 cavity, but this occurs on 100 ns time scale (2–3, 20, 34). The access from the primary site to the permanent Xe binding cavities can be increased by site-directed mutation (37). The fact that CO is transiently trapped

NIH-PA Author Manuscript

NIH-PA Author Manuscript

NIH-PA Author Manuscript

near the heme Fe in SWMb*CO suggests that the B site is occupied only because of the excess thermal energy of photolysis that permits the CO to displace amino acids in the distal pocket. Residues Leu29 and Ile107 surrounding the B state are pushed away by photodissociated CO as CO moves to B state at 100 ps, as evident from the room temperature time-resolved X-ray data (2). Moreover, in the rigid SWMb*CO structure at 40K, CO is initially observed only ~1 Å from its bound location (38). Only after an extended illumination over several hours, CO was observed to gradually shift in the distal pocket to the B site observed in the room temperature time-resolved experiments, about 2.5 Å away from the bound location (39). However, this site is still not the same as the nearest Xe binding site in SWMb (Xe4). These results suggest that there is a constrained distal docking site in Mb, which is absent in DHP. This difference is evident in the appearance of two CO absorption bands in the cryogenic FTIR spectrum of photolyzed SWMb*CO corresponding to the B_1 and B_2 states (40). DHP*CO lacks this features and has one major band in the cryogenic photoproduct spectrum suggesting the CO migrates to a relatively large protein cavity (Xe1) in DHP (33). The behavior of SWMb*CO indicates gating of the ligand motion by the protein, consistent with the fact that SWMb*CO has a sufficiently constrained distal pocket that it cannot accommodate both H_2O and O_2 (or CO) at the same time. Thus, the SWMb distal pocket acts as a valve that permits only one small molecule to transit at a time. DHP lacks this valve and permits CO to move more freely through the distal pocket, as well as to escape much more readily than in SWMbCO.

Molecular Dynamics Simulation of DHP-CO

To examine the dynamics of the CO ligand trajectories, molecular dynamics (MD) simulations were conducted on photolyzed DHP*CO similar to simulations that have been carried out on SWMb*CO and HbI*CO (4, 41–43). MD simulations were carried out for both the δ- and ε-tautomers of the distal histidine, His 55, with a free CO molecule that can migrate from a starting location above the heme Fe prior to equilibration. Figure 4 shows the distances from the CO carbon atom to the heme Fe and key amino acid residues surrounding the Xe1 binding site. During the simulation, the free CO molecule was observed to dwell in the Xe1 binding site for the majority of the simulation time. The distances of the Xe1 binding site in the DHP structure (PDB 3MOU) (13) to the α-carbon of each of the surrounding amino acids are shown as the dotted black lines in the figures. The δ-His tautomer shows more variation in the CO position, which is divided between the Xe binding site and a site in the distal pocket near the heme Fe. The CO ligand leaves the distal pocket after 18 ns and 20 ns in the δ-His and ε-His tautomer, respectively. Given the greater apparent fluctuation of the CO in the δ-tautomer of H55, it is not surprising that the CO escapes an earlier time in that simulation. However, CO escape is relatively rapid in both simulations consistent with the hypothesis that DHP has a more open distal pocket than in other myoglobins and hemoglobins. The behavior is quite different from SWMb*CO, in which the CO is observed in the docking (or B) site and typical escape times are on the order of 100–200 ns (41), i.e. ten times longer than both the measured (33) and simulated times for DHP*CO presented in Figure 4.

Figure 4A shows that, up to the point of CO ligand escape, the average distance Fe-C distance is 7.6 and 6.6Å, for the δ- and ε-tautomer of H55, respectively. Figure 4B shows the complementary aspect of the CO trajectory. Since L100 is in the back of the Xe1 binding cavity furthest from the heme Fe, the correlation of the distances in Figures 4A and 4B shows that the CO fluctuates between a site near the Fe and the Xe1 binding site in the presence of the δ-tautomer. While this close site in DHP*CO is similar in distance to the heme Fe to the B state in SWMb*CO, the behavior is quite different. The CO is not trapped near the Fe in DHP, but rather visits that site as an excursion from the principal location, which is the DHP Xe1 binding site.

NIH-PA Author Manuscript

NIH-PA Author Manuscript

NIH-PA Author Manuscript

Function of cavities in SWMb and HbI as a protection against autooxidation

The role of cavities in SWMb and HbI has been studied in terms of both dynamics and function (2, 4, 44–45). The primary function of both HbI and SWMb is oxygen transport and storage, which requires a Fe^{2+} state for the heme. Hemoglobins, and to a lesser extent myoglobins, in higher organisms are responsive to a large number of allosteric effectors, such as H^+ (the Bohr effect), Cl^-, Ca^{2+}, inositol hexaphosphate and so on, which modulate the release of O_2 (46). While the interior multiple cavities surrounding the heme in HbI and SWMb are not thought to be required for O_2 migration in and out of the protein, they may serve to permit O_2 to be sequestered for some time following release from the heme Fe (or in reverse when entering the protein to bind to the heme Fe) (47). Since the rate of auto-oxidation of oxyferrous SWMb is accelerated by H^+, the hydrophobic interior cavities in SWMb may prevent the attack of H^+ by sequestering O_2 from H_2O (48). Possibly, O_2 passes through the cavities in response to transient entry of H_2O into the distal pocket. Since allosteric effects tune the binding constant, they may also affect the kinetics of migration inside the protein in a manner that is appropriate for the physiological role of the globin. The water entry into the distal pocket of Mb after photodissociated CO migrates into proximal site (22) supports the hypothesis that Mb has a relatively small distal cavity, which serves to separate O_2 from H_2O molecules when O_2 is bound to the heme Fe. Thus, the amino acids in the distal cavity of SWMb act like a valve that controls the diatomic ligand trajectory and isolates it from H_2O, and particularly from H_3O^+, in order to slow the autooxidation rate. The valve significantly impedes ligand diffusion by a second molecule into the distal pocket of SWMb. The autooxidation rate of SWMb increases if the distal pocket is opened by site-directed mutagenesis and conversely is slowed significantly for mutations that further occlude the distal pocket (49).

DHP lacks the multiple Xe binding site structure of SWMb and instead has only one internal Xe binding cavity, Xe1 (13). As shown in Figure 3B, the Xe1 and Xe4 sites in SWMb are blocked by Phe side chains (F97 and F60, respectively) in DHP. Therefore, DHP does not provide the extensive set of protein cavities observed in HbI and SWMb. Nor does DHP have the degree of steric constraint near the heme Fe atom seen SWMb and HbI. Therefore, photodissociated CO migrates into DHP Xe1 cavity without any hindrance. Moreover, CO can rapidly recombine from the Xe1 site as shown in Figure 1. It is evident that the distal pocket of DHP is larger than that of SWMb since there are X-ray crystal structures and spectroscopy data which show that a range of 4-halophenols and 2,4,6-trihalophenols bind in the distal pocket of DHP (15, 35, 50). The studies of SWMb with relatively large isocyanates in the distal pocket represent a qualitatively different mode of binding since those molecules are all bound to the heme Fe (51). Crystallographic studies of isocyanide binding in Mb have provided information on entry/exit pathways for diatomic ligands (51–52). Although these are considered large molecules, the volume of the n-butyl group (the largest in the series) is still ~30% smaller than that of 2,4,6-TBP, which is the native substrate of DHP.

DHP is not susceptible to autooxidation because of its high Fe(III)/Fe(II) reduction potential (53). In fact, DHP has a reduction potential of $E° = +204$ mV, which is the highest of any monomeric hemoglobin or myoglobin studied to date (53). The very high redox potential indicates that Fe(II) is favored over Fe(III) under physiological conditions. Consequently, DHP has such a low autooxidation rate that it appears not to require the same safeguards as SWMb to protect against protonation of bound O_2. For this reason we hypothesize that SWMb and other similar globins require a valve that permits O_2 to bind and unbind without any contact with other small molecules. However, unlike these globins DHP must have an open distal pocket, lacking the kind of small-molecule valve found in SWMb, since the DHP mechanism requires the initiation of catalysis requires displacement of bound O_2 by H_2O_2. Thus, both molecules must be simultaneously present in the distal pocket (16). Such a mechanism would

NIH-PA Author Manuscript

NIH-PA Author Manuscript

NIH-PA Author Manuscript

be impossible in SWMb and other globins since the valve would only permit one of the two molecules into the distal pocket at any given time.

Conclusion

The time-resolved X-ray structural data presented in Figure 1 show that single Xe-binding in DHP is correlated with the bifunctional property of DHP: oxygen storage and peroxidase activity. The distal cavity in DHP has an open structure consistent with its capacity to bind both 4-BP and 2,4,6-TBP in different internal sites (35). The distal Xe binding site appears to play a key role in stabilizing the binding of 4-BP (13). Moreover, substrate binding at a different internal site has been observed to trigger the H_2O_2 displacement reaction at the heme Fe (16). The occupation of the Xe-binding site by CO observed in the time-resolved X-ray data suggests that this site could be transiently occupied by H_2O_2 prior to displacing the O_2 bound to the heme Fe. The fact that photolyzed CO occupies the Xe1 binding site and rapidly recombines with the heme Fe reveals how facile it would be for an H_2O_2 molecule to exchange with O_2 from this site. Once that has occurred O_2 could escape into the solvent from the Xe1 binding site. Thus, time-resolved X-ray crystallography reveals important functional differences in globins specialized for O_2 transport and storage and those that can have auxiliary functions in detoxification. Simple organisms such *A. ornata* have no liver or other organ that specializes in detoxification, and thus it appears that the dehaloperoxidase-hemoglobin is a multifunctional protein that has evolved to provide both O_2 transport and detoxification functions. The present study shows that time-resolved X-ray crystallography has tremendous potential for elucidating function based on characteristic differences in the photolyzed CO dynamics.

Supplementary Material

Refer to Web version on PubMed Central for supplementary material.

References

1. Srajer V, Teng TY, Ursby T, Pradervand C, Ren Z, Adachi S, Schildkamp W, Bourgeois D, Wulff M, Moffat K. Photolysis of the carbon monoxide complex of myoglobin: Nanosecond time-resolved crystallography. Science. 1996; 274:1726–1729. [PubMed: 8939867]
2. Schotte F, Lim MH, Jackson TA, Smirnov AV, Soman J, Olson JS, Phillips GN, Wulff M, Anfinrud PA. Watching a protein as it functions with 150-ps time-resolved X-ray crystallography. Science. 2003; 300:1944–1947. [PubMed: 12817148]
3. Schmidt M, Nienhaus K, Pahl R, Krasselt A, Anderson S, Parak F, Nienhaus GU, Srajer V. Ligand migration pathway and protein dynamics in myoglobin: A time-resolved crystallographic study on L29W MbCO. Proc Natl Acad Sci U S A. 2005; 102:11704–11709. [PubMed: 16085709]
4. Knapp JE, Pahl R, Cohen J, Nichols JC, Schulten K, Gibson QH, Srajer V, Royer WE. Ligand Migration and Cavities within Scapharca Dimeric Hbl: Studies by Time-Resolved Crystallography, Xe Binding, and Computational Analysis. Structure. 2009; 17:1494–1504. [PubMed: 19913484]
5. Knapp JE, Pahl R, Srajer V, Royer WE. Allosteric action in real time: Time-resolved crystallographic studies of a cooperative dimeric hemoglobin. Proc Natl Acad Sci U S A. 2006; 103:7649–7654. [PubMed: 16684887]
6. Scott EE, Gibson QH, Olson JS. Mapping the pathways for O2 entry into and exit from myoglobin. J Biol Chem. 2001; 276:5177–5188. [PubMed: 11018046]
7. Olson JS, Soman J, Phillips GN. Ligand pathways in myoglobin: A review of trp cavity mutations. IUBMB Life. 2007; 59:552–562. [PubMed: 17701550]
8. Nienhaus GU, Nienhaus K. Infrared study of carbon monoxide migration among internal cavities of myoglobin mutant L29W. Journal of Biological Physics. 2002; 28:163–172. [PubMed: 23345766]
9. Nienhaus K, Deng PC, Kriegl JM, Nienhaus GU. Structural dynamics of myoglobin: Spectroscopic and structural characterization of ligand docking sites in myoglobin mutant L29W. Biochemistry. 2003; 42:9633–9646. [PubMed: 12911305]

NIH-PA Author Manuscript

NIH-PA Author Manuscript

NIH-PA Author Manuscript

10. Nienhaus K, Ostermann A, Nienhaus GU, Parak FG, Schmidt M. Ligand migration and protein fluctuations in myoglobin mutant L29W. Biochemistry. 2005; 44:5095–5105. [PubMed: 15794647]
11. Nienhaus K, Knapp JE, Palladino P, Royer WE, Nienhaus GU. Ligand Migration and Binding in the Dimeric Hemoglobin of *Scapharca inaequivalvis*. Biochemistry. 2007; 46:14018–14031. [PubMed: 18001141]
12. Steinbach PJ, Ansari A, Berendzen J, Braunstein D, Chu K, Cowen BR, Ehrenstein D, Frauenfelder H, Johnson JB, Lamb DC, Luck S, Mourant JR, Nienhaus GU, Ormos P, Philipp R, Xie A, Young RD. Ligand binding to heme proteins: connection between dynamics and function. Biochemistry. 1991; 30:3988–4001. [PubMed: 2018767]
13. de Serrano V, Franzen S. Structural Evidence for Stabilization of Inhibitor Binding by a Protein Cavity in the Dehaloperoxidase-Hemoglobin from Amphitrite ornata. Peptide Sci. 2012; 98:27–35.
14. Chen YP, Woodin SA, Lincoln DE, Lovell CR. An unusual dehalogenating peroxidase from the marine terebellid ploychaete Amphitrite ornata. J Biol Chem. 1996; 271
15. Thompson MK, Ghiladi RA, Franzen S. The Dehaloperoxidase Paradox. Biochim Biophys Acta. 2012; 1842:578–588. [PubMed: 22248447]
16. D'Antonio J, Ghiladi RA. Reactivity of Deoxy- and Oxyferrous Dehaloperoxidase B from Amphitrite ornata: Identification of Compound II and Its Ferrous-Hydroperoxide Precursor. Biochemistry. 2011; 50:5999–6011. [PubMed: 21619067]
17. Du J, Sono M, Dawson JH. Functional Switching of Amphitrite ornata Dehaloperoxidase from O_2 Binding Globin to Peroxidase Enzyme Facilitated by Halophenol Substrate and H_2O_2. Biochemistry. 2010; 49:6064–6069. [PubMed: 20565134]
18. Dunford, BH. Heme Peroxidases. John Wiley and Sons; New York: 1999.
19. Gumiero A, Murphy EJ, Metcalfe CL, Moody PCE, Raven EL. An analysis of substrate binding interactions in the heme peroxidase enzymes: A structural perspective. Archives of Biochemistry and Biophysics. 2010; 500:13–20. [PubMed: 20206594]
20. Schotte F, Soman J, Olson JS, Wulff M, Anfinrud PA. Picosecond time-resolved X-ray crystallography: probing protein function in real time. Journal of Structural Biology. 2004; 147:235–246. [PubMed: 15450293]
21. Cao WX, Christian JF, Champion PM, Rosca F, Sage JT. Water penetration and binding to ferric myoglobin. Biochemistry. 2001; 40:5728–5737. [PubMed: 11341838]
22. Goldbeck RA, Bhaskaran S, Ortega C, Mendoza JL, Olson JS, Soman J, Kliger DS, Esquerra RM. Water and ligand entry in myoglobin: Assessing the speed and extent of heme pocket hydration after CO photodissociation. Proc Natl Acad Sci USA. 2006; 103:1254–1259. [PubMed: 16432219]
23. Graber T, Anderson S, Brewer H, Chen YS, Cho HS, Dashdorj N, Henning RW, Kosheleva I, Macha G, Meron M, Pahl R, Ren Z, Ruan S, Schotte F, Rajer VS, Viccaro PJ, Westferro F, Anfinrud P, Moffat K. BioCARS: a synchrotron resource for time-resolved X-ray science. J Synchrotron Rad. 2011; 18:658–670.
24. Ren, Z. Precognition User Guide. RenZ Research Inc; Illinois, USA: 2010.
25. Krissinel EB, Winn MD, Ballard CC, Ashton AW, Patel P, Potterton EA, McNicholas SJ, Cowtan KD, Emsley P. The new CCP4 Coordinate Library as a toolkit for the design of coordinate-related applications in protein crystallography. Acta Crystallogr, Sect D: Biol Crystallogr D60. 2004:2250–2255.
26. Potterton L, McNicholas S, Krissinel E, Gruber J, Cowtan K, Emsley P, Murshudov GN, Cohen S, Perrakis A, Noble M. Developments in the CCP4 molecular-graphics project. Acta Crystallogr, Sect D: Biol Crystallogr D60. 2004:2288–2294.
27. Ren Z, Perman B, Srajer V, Teng TY, Pradervand C, Bourgeois D, Schotte F, Ursby T, Kort R, Wulff M, Moffat K. A molecular movie at 1.8 angstrom resolution displays the photocycle of photoactive yellow protein, a eubacterial blue-light receptor, from nanoseconds to seconds. Biochemistry. 2001; 40:13788–13801. [PubMed: 11705368]
28. McRee, D. Practical Protein Crystallography. Academic Press; San Diego, CA: 1993.
29. Phillips JC, Braun R, Wang W, Gumbart J, Tajkhorshid E, Villa E, Chipot C, Skeel RD, Kale L, Schulten K. Scalable molecular dynamics with NAMD. J Comp Chem. 2005; 26:1781–1802. [PubMed: 16222654]

NIH-PA Author Manuscript

NIH-PA Author Manuscript

NIH-PA Author Manuscript

30. Andersen HC. Rattle: A “velocity” version of the shake algorithm for molecular dynamics calculations. Journal of Computational Physics. 1983; 52:24–34.
31. Sagui C, Darden T. Multigrid methods for classical molecular dynamics simulations of biomolecules. The Journal of Chemical Physics. 2001; 114:6578–6591.
32. de Serrano V, Chen ZX, Davis MF, Franzen S. X-ray crystal structural analysis of the binding site in the ferric and oxyferrous forms of the recombinant heme dehaloperoxidase cloned from Amphitrite ornata. Acta Crystallogr, Sect D: Biol Crystallogr. 2007; 63:1094–1101. [PubMed: 17881827]
33. Nienhaus K, Deng P, Belyea J, Franzen S, Nienhaus GU. Spectroscopic Study of Substrate Binding to the Carbonmonoxy Form of Dehaloperoxidase from Amphitrite ornata. J Phys Chem B. 2006; 110:13264–13276. [PubMed: 16805641]
34. Srajer V, Ren Z, Teng TY, Schmidt M, Ursby T, Bourgeois D, Pradervand C, Schildkamp W, Wulff M, Moffat K. Protein conformational relaxation and ligand migration in myoglobin: A nanosecond to millisecond molecular movie from time-resolved Laue X-ray diffraction. Biochemistry. 2001; 40:13802–13815. [PubMed: 11705369]
35. Zhao J, de Serrano V, Zhao J, Le P, Franzen S. Structural and kinetic study of an internal substrate binding site in dehaloperoxidase-hemoglobin A from Amphitrite ornata. Biochemistry. 2013; 52:2427–2439. [PubMed: 23480178]
36. Tilton RF Jr, Kuntz ID Jr, Petsko GA. Cavities in proteins: structure of a metmyoglobin xenon complex solved to 1.9 Ã…. Biochemistry. 1984; 23:2849–2857. [PubMed: 6466620]
37. Brunori M, Vallone B, Cutruzzola F, Travaglini-Allocatelli C, Berendzen J, Chu K, Sweet RM, Schlichting I. The role of cavities in protein dynamics: Crystal structure of a photolytic intermediate of a mutant myoglobin. Proceedings of the National Academy of Sciences of the United States of America. 2000; 97:2058–2063. [PubMed: 10681426]
38. Teng T-Y, Srajer V, Moffat K. Photolysis-induced structural changes in single crystals of carbonmonoxy myoglobin at 40 K. Nature Structural Biology. 1994; 1:701–705.
39. Teng TY, Srajer V, Moffat K. Initial trajectory of carbon monoxide after photodissociation from myoglobin at cryogenic temperatures. Biochemistry. 1997; 36:12087–12100. [PubMed: 9315847]
40. Lim MH, Jackson TA, Anfinrud PA. Ultrafast rotation and trapping of carbon monoxide dissociated from myoglobin. Nat Struct Biol. 1997; 4:209–214. [PubMed: 9164462]
41. Meller J, Elber R. Computer simulations of carbon monoxide photodissociation in myoglobin: Structural interpretation of the B states. Biophys J. 1998; 74:789–802. [PubMed: 9533692]
42. Elber R. Ligand diffusion in globins: simulations versus experiment. Curr Opin Struct Biol. 2010; 20:162–167. [PubMed: 20116995]
43. Ruscio JZ, Kumar D, Shukla M, Prisant MG, Murali TM, Onufriev AV. Atomic level computational identification of ligand migration pathways between solvent and binding site in myoglobin. Proc Natl Acad Sci USA. 2008; 105:9204–9209. [PubMed: 18599444]
44. Frauenfelder H, McMahon BH, Austin RH, Chu K, Groves JT. The role of structure, energy landscape, dynamics, and allostery in the enzymatic function of myoglobin. Proceedings of the National Academy of Sciences of the United States of America. 2001; 98:2370–2374. [PubMed: 11226246]
45. Beece D, Eisenstein L, Frauenfelder H, Good D, Marden MC, Reinisch L, Reynolds AH, Sorensen LB, Yue KT. Solvent viscosity and Protein Dynamics. Biochemistry. 1980; 19:5147–5157. [PubMed: 7448161]
46. Perutz MF, Wilkinson AJ, Paoli M, Dodson GG. The stereochemical mechanism of the cooperative effects in hemoglobin revisited. Annu Rev Biophys Biomol Struct. 1998; 27:1–34. [PubMed: 9646860]
47. Cohen J, Schulten K. O-2 migration pathways are not conserved across proteins of a similar fold. Biophysical Journal. 2007; 93:3591–3600. [PubMed: 17693478]
48. Brantley RE, Smerdon SJ, Wilkinson AJ, Singleton EW, Olson JS. The mechanism of autooxidation in myoglobin. J Biol Chem. 1993; 268:6995–7010. [PubMed: 8463233]
49. Carver TE, Brantley RE Jr, Singleton EW, Arduini RM, Quillin ML, Phillips GN Jr, Olson JS. A novel site-directed mutant of myoglobin with an unusually high O_2 affinity and low autooxidation rate. J Biol Chem. 1992; 267:14443–14450. [PubMed: 1629229]

NIH-PA Author Manuscript

NIH-PA Author Manuscript

NIH-PA Author Manuscript

50. Nienhaus K, Nickel E, Davis MF, Franzen S, Nienhaus GU. Determinants of Substrate Internalization in the Distal Pocket of Dehaloperoxidase Hemoglobin of Amphitrite ornata. Biochemistry. 2008; 47:12985–12994. [PubMed: 19006323]

51. Johnson KA, Olson JS, Phillips GN jr. Structure of myoglobin-ethyl isocyanide histidine as a swinging door for ligand entry. Journal of Molecular Biology. 1989; 207:459–463. [PubMed: 2754735]

52. Smith RD, Blouin GC, Johnson KA, Phillips GN, Olson JS. Straight-Chain Alkyl Isocyanides Open the Distal Histidine Gate in Crystal Structures of Myoglobin. Biochemistry. 2010; 49:4977–4986. [PubMed: 20481504]

53. D'Antonio EL, Bowden EF, Franzen S. Thin-layer spectroelectrochemistry of the Fe(III)/Fe(II) redox reaction of dehaloperoxidase-hemoglobin. J Electroanal Chem. 2012; 668:37–43.

NIH-PA Author Manuscript

NIH-PA Author Manuscript

NIH-PA Author Manuscript

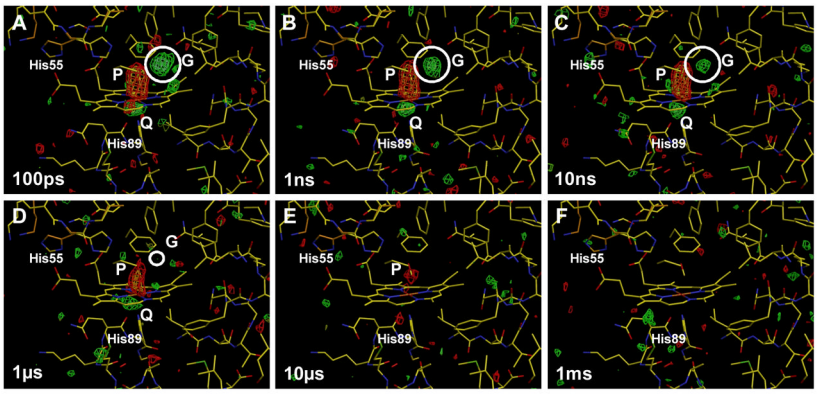

Figure 1.

Weighted difference light-dark Fourier maps of the heme region (subunit A) of DHP-CO at different time delays after the laser pulse. The maps are calculated at 1.8 Å resolution as described in Methods section. Light green and green signify positive difference electron densities, while orange and red signify negative densities. Two contouring levels are shown for both positive and negative densities: ±3σ and ±5σ. The outer, darker colors (red and green) represent ±3σ contours. The inner, lighter colors (orange and light green) represent ±5σ contours (σ is the root-mean-square value of the difference density over the asymmetric unit). (A) 100 ps delay; (B) 1ns delay; (C) 10 ns delay; (D) 1 us delay; (E) 10 us delay; (F) 1 ms delay. The positive density in the circle, labeled G, shows the primary docking site of dissociated CO. Negative density P and positive density Q correspond to the loss of CO upon photolysis and the motion of Fe out of heme plane toward proximal histidine when CO dissociates, respectively.

NIH-PA Author Manuscript

NIH-PA Author Manuscript

NIH-PA Author Manuscript

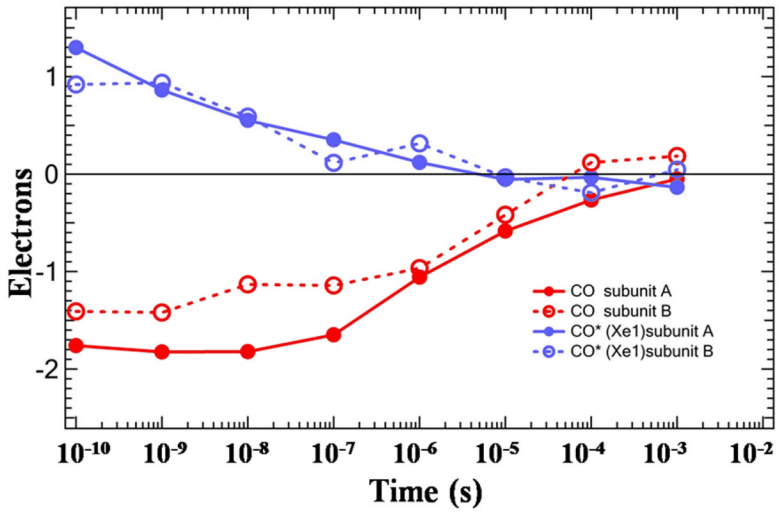

Figure 2.

Time courses for integrated difference electron densities in F_o(DHP*CO) - F_o(DHP-CO) maps for subunits A and B of DHP. The red traces represent the CO heme Fe binding site (site P) and the blue traces correspond to the CO in the Xe1 binding site (site G).

NIH-PA Author Manuscript

NIH-PA Author Manuscript

NIH-PA Author Manuscript

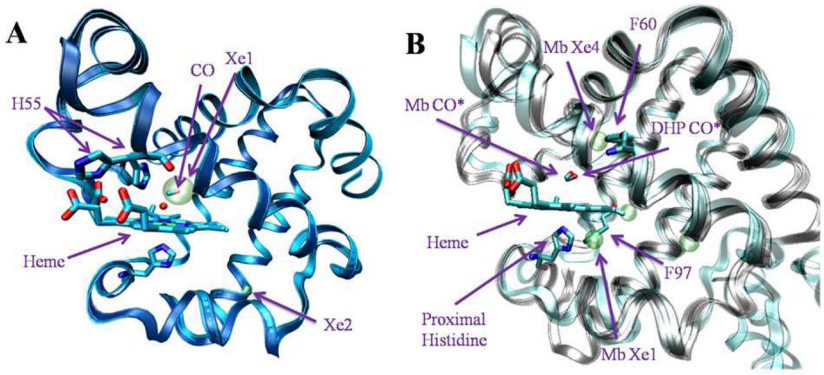

Figure 3.

A: Ribbon diagram of the overlaid metaquo structure of DHP derivatized with Xe (PDB 3MOU, cyan), and DHP-CO structure (blue). The two Xe binding sites are occupancy weighted in the figure (Xe1 = 0.4; Xe2 = 0.1). The water molecule above heme Fe is present only in the metaquo-DHP structure. The bound CO molecule in DHP-CO is not shown. Instead, a location of the CO molecule after photolysis is shown, based on the positive density at the Xe 1 binding site in the 100ps and 1ns difference electron density maps (Fig. 1). B: Ribbon diagram of the overlaid structures of the DHP-CO (in cyan; bound CO molecule not shown; location of photodissociated CO shown), SWMb*CO B site (PDB 2G0V, in grey) and SWMb derivatized with Xe (PDB 2W6W, in grey). The location of photodissociated CO is based on the location of positive CO density in 100ps and 1ns difference maps. Location of photodisociated CO at site B in SWMb*CO (based on the location of positive CO density in 100 ps difference map) is also shown, indicating nearly the same initial location of the photodissociated CO in two molecules. Green spheres indicate locations of four Xe cavities in SWMb.

NIH-PA Author Manuscript
NIH-PA Author Manuscript
NIH-PA Author Manuscript

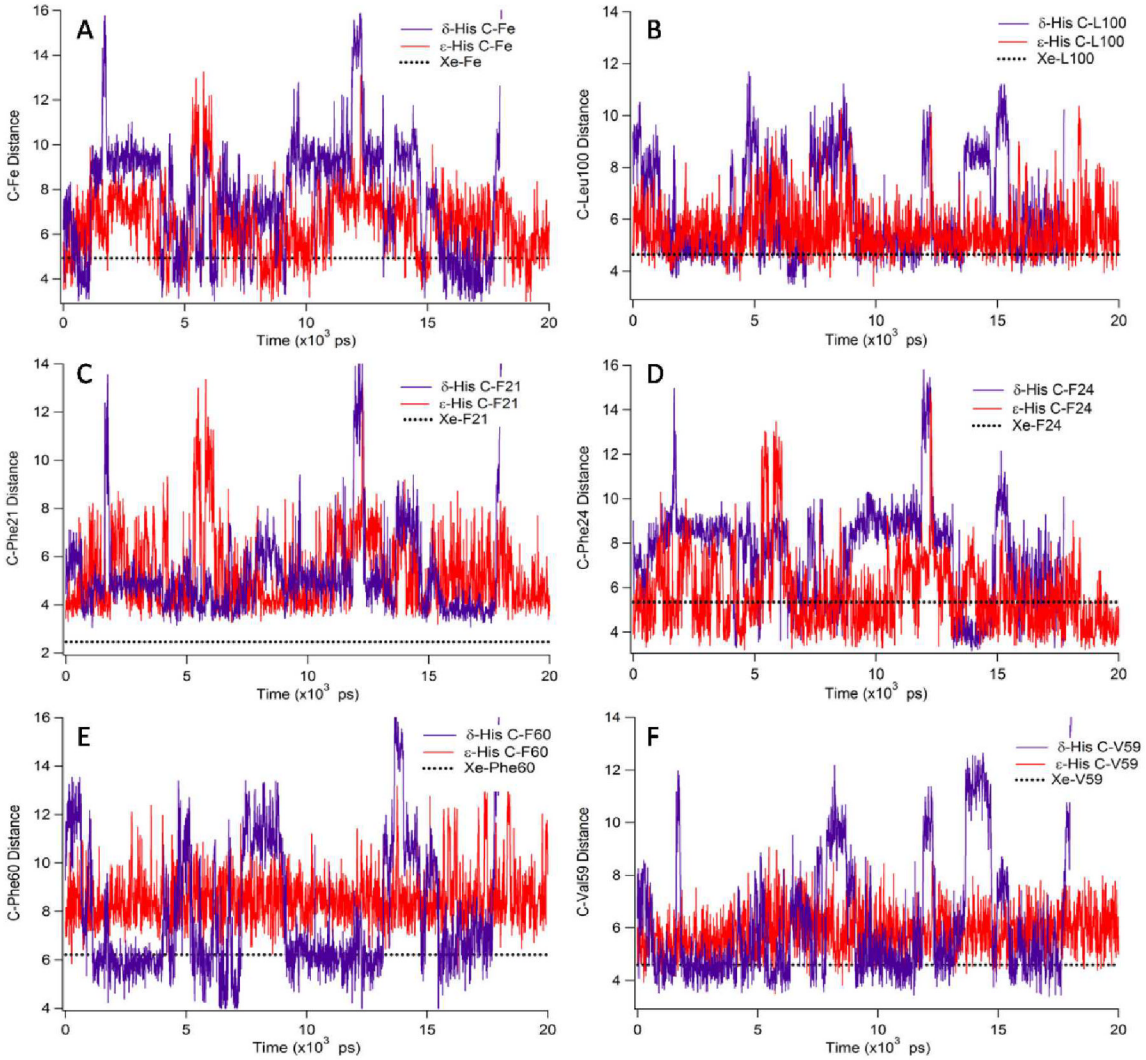

Figure 4.

Distances (in Å) from the dissociated CO carbon atom to the heme Fe and key amino acid residues surrounding the Xe1 binding site as a function of time during MD simulation. A) Distance from the CO carbon to the heme; B) Distance from the CO carbon to Leu 100; C) Distance from the CO carbon to Phe 21;D) Distance from the CO carbon to Phe 24; E) Distance from the CO carbon to Phe 60; F) Distance from the CO carbon to Val 59.